

## Jet Breaks in Short Gamma-Ray Bursts. II: The Collimated Afterglow of GRB 051221A

David N. Burrows<sup>1</sup>, Dirk Grupe<sup>1</sup>, Milvia Capalbi<sup>2</sup>, Alin Panaitescu<sup>3</sup>, Sandeep K. Patel<sup>4,5</sup>, Chryssa Kouveliotou<sup>5</sup>, Bing Zhang<sup>6</sup>, Peter Mészáros<sup>1,7</sup>, Guido Chincarini<sup>8,9</sup>, Neil Gehrels<sup>10</sup>, Ralph A.M. Wijers<sup>11</sup>

### ABSTRACT

We report the best evidence to date of a jet break in a short Gamma-Ray Burst (GRB) afterglow, using *Chandra* and *Swift* XRT observations of the X-ray afterglow of GRB 051221A. The combined X-ray light curve, which has three breaks, is similar to those commonly observed in *Swift* observations of long GRBs. A flat segment of the light curve at  $\sim 0.1$  days after the burst represents the first clear case of strong energy injection in the external shock of a short GRB afterglow. The last break in the light curve occurs at  $\sim 4$  days post-burst and breaks to a power-law decay index of  $\sim 2$ . We interpret this as a jet break, with important implications for models of short GRBs, since it requires collimation of the afterglow into a jet with an initial opening angle  $\theta_0 \sim 4^\circ - 8^\circ$  and implies a

---

<sup>1</sup>Department of Astronomy and Astrophysics, Pennsylvania State University, 525 Davey Lab, University Park, PA 16802; [burrows@astro.psu.edu](mailto:burrows@astro.psu.edu)

<sup>2</sup>ASI Science Data Center, via Galileo Galilei, 00044 Frascati, Italy

<sup>3</sup>Space Science and Applications, MS D466, Los Alamos National Laboratory, Los Alamos, NM 87545

<sup>4</sup>Universities Space Research Association, 10211 Wincopin Circle, Suite 500, Columbia, MD 21044-3432

<sup>5</sup>NASA/Marshall Space Flight Center, National Space Science Technology Center, VP-62, 320 Sparkman Dr., Huntsville, AL 35805

<sup>6</sup>Department of Physics, University of Nevada, Las Vegas, NV 89154

<sup>7</sup>Department of Physics, Pennsylvania State University, University Park, PA 16802

<sup>8</sup>INAF – Osservatorio Astronomico di Brera, Via Bianchi 46, 23807 Merate, Italy

<sup>9</sup>Università degli studi di Milano-Bicocca, Dipartimento di Fisica, Piazza delle Scienze 3, I-20126 Milan, Italy

<sup>10</sup>NASA Goddard Space Flight Center, Greenbelt, MD 20771

<sup>11</sup>Astronomical Institute 'Anton Pannekoek', University of Amsterdam, Kruislaan 403, NL-1098 SJ Amsterdam, The Netherlands

total jet kinetic energy of  $E_{jet} \sim (1 - 5) \times 10^{49}$  erg. Combined with the lack of a jet break in GRB 050724, this suggests a wide range in jet collimation in short GRBs, with at least some having collimation similar to that found in long GRBs, though with significantly lower jet energies.

*Subject headings:* gamma rays: bursts

## 1. Introduction

Until recently, afterglows of short Gamma-Ray Bursts have proven to be extremely elusive, frustrating efforts to identify their progenitors and environments. This situation changed dramatically in 2005. The *Swift* (Gehrels et al. 2004) Burst Alert Telescope (BAT; Barthelmy et al. 2005a) localized 11 short Gamma-Ray Bursts (GRBs) between 2005 February 1 and 2006 January 31, and the *Swift* X-Ray Telescope (XRT; Burrows et al. 2005) identified X-ray afterglows from six of these (two could not be observed by the XRT, and the rest were too faint to detect). These observations led to the first precise localization of a short GRB, GRB 050509B, and the discovery that it was probably located in a giant elliptical galaxy with extremely low star formation (Gehrels et al. 2005; Hjorth et al. 2005b; Bloom et al. 2006), lending support to a merger model for short bursts (e.g. Lattimer & Schramm 1976; Paczyński 1986; Eichler et al. 1989; Paczyński 1991; Rosswog, Ramirez-Ruiz, & Davies 2003; Rosswog 2005). This picture was confirmed two months later by the *HETE-II* discovery of the short GRB 050709 (Villasenor et al. 2005) and its localization to a region of low star formation (Hjorth et al. 2005a; Fox et al. 2005); and by the *Swift* discovery of the short GRB 050724 (Barthelmy et al. 2005b; Campana et al. 2006) in another elliptical galaxy.

Of the six short bursts localized by the XRT, only three were bright enough in X-rays to permit detailed study: GRB 050724, GRB 051221A, and GRB 051227 (Barbier et al. 2006). *Chandra* followup observations obtained for GRB 050724 and for GRB 051221A are critical for constraining jet breaks in both bursts. GRB 050724 is discussed in a companion paper (Grupe et al. 2006, Paper I). In this paper we discuss the late X-ray afterglow of GRB 051221A as observed by the XRT and by the *Chandra* ACIS-S instrument. We show that a break is observed in the late-time X-ray light curve. If interpreted as a jet break, these observations provide a measurement of the jet opening angle, and hence allow us to determine the jet energy for this short burst.

We characterize the dependence of the X-ray flux on time and frequency as  $F(t, \nu) \propto (t - T_0)^{-\alpha} \nu^{-\beta}$ , where  $T_0$  is the time of the BAT trigger,  $\alpha$  is the decay index, and  $\beta$  is the spectral

energy index. Error bars on data points are  $1\sigma$ , while those given for model parameters are 90% confidence limits for one interesting parameter ( $\chi^2_{min} + 2.7$ ) unless otherwise specified. We use standard  $\Lambda$ CDM cosmological parameters of  $\Omega_M=0.27$ ,  $\Omega_\Lambda=0.73$  and  $H_0=71$  km s $^{-1}$  Mpc $^{-1}$ .

## 2. Observations and Data Reduction

GRB 051221A was detected by the *Swift*/BAT at  $T_0=01:51:16$  UT on 21 December 2005 (Parsons et al. 2005). The burst was a short, hard burst, with  $T_{90} = 1.4 \pm 0.2$  s and a hard photon index in the 15-150 keV band of  $\Gamma = 1.39 \pm 0.06$  (Cummings et al. 2005). The Konus-Wind instrument measured a cut-off power law spectrum with  $E_{peak} = 402^{+93}_{-72}$  keV (Golenetskii et al. 2005). The 15–150 keV fluence was  $1.16 \pm 0.04 \times 10^{-6}$  ergs cm $^{-2}$  (Cummings et al. 2005), making this the most fluent BAT-detected short burst yet, by a factor of two.

The *Swift*/XRT observations of GRB 051221A began at 01:52:44 UT, 88 seconds after the BAT trigger. The XRT was not able to determine a centroid on-board because of insufficient counts in the 2.5 second Image Mode exposure (see Hill et al. 2004, for a description of the XRT readout modes). Data were taken primarily in Windowed Timing mode from  $T_0 + 93$  s until about  $T_0 + 300$  s, after which the instrument switched to Photon-Counting (PC) mode. Subsequent ground analysis of the PC mode data provided a position with  $3''.5$  uncertainty (Burrows, Capalbi, & Grupe 2005). XRT observations continued until 2006 January 3 (13.7 days after the trigger), although the source became undetectable by XRT after about 11 days post-burst, and only upper limits are available at later times.

The XRT data were reduced with the XRTDAS tools included in the HEASoft 6.0.4 package, using the latest calibration files available in CALDB and applying standard data screening. For the WT mode data, events in the 0.3–10 keV band with grades 0–2 were used in the analysis (see Burrows et al. 2005, for XRT event grade definitions). For the PC mode data, we selected events in the same energy range with grades 0–12.

The GRB afterglow was located near a hot column on the CCD. The position on the detector changes with each orbit, leading to a significant loss of effective area for some orbits during which the PSF core falls partially on the columns that are masked off by the analysis software. In order to minimize the impact on our data analysis, we used a small data extraction region (a 5 pixel radius circle in PC mode and a 10 pixel box width in WT mode), correcting the derived count rates for the fraction of the PSF included in the extraction regions. (The plate scale is  $2''.34$  per pixel.) When the hot columns penetrated

the extraction region we used a larger extraction area (10 pixel radius circle) and calculated exposure maps, excluding the hot columns and adjacent columns, to make the necessary corrections to the count rates. These corrections ranged up to a factor of 1.9 for some orbits.

Data in the first 200 s of PC mode, when the source count rate exceeds  $\sim 0.5$  counts  $s^{-1}$ , were affected by pile-up, and were corrected by excluding events within a circle of 2 pixels radius around the afterglow (see Vaughan et al. 2006; Pagani et al. 2006; Romano et al. 2006, for details of pile-up correction procedures for XRT data). Again, these effective area losses were taken into account in calculating the light curve. The background used in each mode for both light curve and spectral analysis was estimated from nearby source-free regions.

The *Chandra* Observatory performed five Target of Opportunity observations with the ACIS-S3 CCD under our AO7 observing program, spanning the interval from  $T_0 + 1.2 \times 10^5$  s to  $T_0 + 2.3 \times 10^6$  s. The observing log is given in Table 1. The first two *Chandra* observations overlap the *Swift*/XRT data and provide valuable spectral information at late times, when the count rate in the XRT is too low for spectroscopy. The last three *Chandra* data points extend the X-ray light curve of GRB 051221A out to 16 January 2006. The observations were performed in Faint or Very Faint mode with the standard 3.2 s frame time. Data were reduced using version 3.3 of the CIAO software with CALDB version 3.2.1. Events from the GRB afterglow were selected using a source extraction radius of  $R = 1''.75$  for the 2005 December observations and  $R = 1''.0$  for the 2006 January observations. Background regions were chosen from a source-free area using a radius 10 times larger than the source region.

### 3. Data Analysis

#### 3.1. Position

A preliminary *Chandra* position for the afterglow was given in Grupe et al. (2005), based on the standard *Chandra* attitude solution, which is typically good to about  $0''.5$ . We have improved the astrometry of the first *Chandra* observation by reference to the 2MASS system. The *Chandra*/ACIS data were reprocessed with pixel randomization turned off in order to provide the most accurate positions. We find 33 X-ray sources on CCDs S2 and S3 within 6 arcminutes of the GRB position with signal-to-noise ratio greater than 2.7. These were matched to the 2MASS catalog to look for near-IR counterparts, resulting in 6 potential matches. Two of these were found to have large offsets and were discarded as unrelated position coincidences. We were left with 4 optical counterparts to X-ray sources, all with offsets less than  $1\sigma_{PSF}$ . Averaging the offsets between the *Chandra* and 2MASS

positions for these four objects, we find astrometry corrections of  $-0''.094$  in right ascension and  $+0''.015$  in declination. We applied these offsets to the best-fit *Chandra* position (using a circular Gaussian fit to the image) to obtain the final position of the X-ray afterglow:

$$(\alpha, \delta)_{J2000} = (21^{\text{h}}54^{\text{m}}48^{\text{s}}.620, +16^{\circ}53'27''.19).$$

The RMS residuals are  $0''.17$  in RA and  $0''.25$  in declination. This position is  $0''.28$  arcseconds from the optical afterglow (Soderberg et al. 2006), which was calibrated relative to the USNO-B system and has  $0''.18$  rms uncertainty in each coordinate. We note that the optical observations are better-suited to determining the offset of the GRB from its host galaxy, which we do not detect with *Chandra*; this offset is given by Soderberg et al. (2006) as  $0''.12 \pm 0''.04$ . The XRT and *Chandra* positions are shown overlaid on a UVOT UVW1 band image in Figure 1.

### 3.2. Spectral Analysis

XRT spectra were accumulated from the WT mode data and from the PC mode data. In the latter case, only data from  $T_0 + 501$  s to  $T_0 + 65721$  s were used, as the earlier PC mode data suffered from pile-up, which distorts spectral fits. Data were binned to have at least 20 counts per bin and were fitted to an absorbed power law, using *XSPEC* version 12.2.1 with version 007 (20060104) of the XRT response matrices. Results of the spectral fits are given in Table 2. From the PC mode spectrum, which is averaged over the first three segments of the light curve, we find an excellent fit to an absorbed power law with photon index  $\Gamma = 2.1 \pm 0.2$  and  $N_{\text{H}} = (1.8_{-0.5}^{+0.7}) \times 10^{21} \text{ cm}^{-2}$  ( $\chi^2 = 13.5$  for 30 degrees of freedom). These results are in good agreement with those from the WT mode spectrum, which has fewer counts and larger uncertainties. The absorbing column density is  $\sim 2\sigma$  higher than the Galactic value of  $6.7 \times 10^{20} \text{ cm}^{-2}$ .

The *Chandra* spectra were analyzed using *XSPEC* version 12.2.1, with data binned to have at least 20 photons per energy bin. Spectral fit results for absorbed power laws are given in Table 2 for the first two *Chandra* observations individually and for their combined spectrum. For the combined spectrum, we obtained an excellent fit with photon index  $\Gamma = 1.94_{-0.19}^{+0.29}$  and  $N_{\text{H}} = (1.4 \pm 0.9) \times 10^{21} \text{ cm}^{-2}$  ( $\chi^2 = 17.2$  for 22 degrees of freedom). These results are in good agreement with the *Swift*/XRT spectral results, indicating no change in spectral parameters from the early portion of the light curve to the late portion at  $\sim 10^5$  s post-burst.

### 3.3. Light curve

Using the best fit spectral parameters for the XRT data, we obtained a mean exposure-corrected conversion factor between XRT count rate and unabsorbed source flux in the 0.3–10 keV band of  $7.9 \times 10^{-11}$  (erg cm<sup>-2</sup> s<sup>-1</sup>)/(count s<sup>-1</sup>) for this afterglow, taking into account the fraction of the PSF contained within the source extraction region. The XRT light curve shown in Figure 2 was generated by multiplying the background-subtracted XRT count rate by the energy conversion factor (ECF) appropriate for each orbit of data (since the exposure varies as described in §2). A similar procedure was used to convert the *Chandra* count rates to flux units, using the *Chandra* spectral fit results discussed in §3.2 to calculate the *Chandra*/ACIS-S ECF for this source,  $1.07 \times 10^{-11}$  erg cm<sup>-2</sup> count<sup>-1</sup>. Table 3 gives the fluxes and uncertainties for all the X-ray data points from Figure 2. For times periods before about 100 ks, our XRT fluxes are systematically about 40% higher than those reported by Soderberg et al. (2006), with better agreement at later times.

As shown in Figure 2, the XRT light curve can be approximated as two power law segments of roughly equal slope separated by a flatter segment. The best-fit power law slope for the data from  $T_0 + 100$  s to  $T_0 + 2200$  s is  $1.09_{-0.10}^{+0.15}$ , while the third segment (from  $3 \times 10^4 - 3.6 \times 10^5$  s) has a best-fit decay index of  $1.19 \pm 0.06$ . The afterglow becomes undetectable in the XRT after 11 days, but the *Chandra* observations at later times show clear evidence for a deviation from the earlier power-law slope.

Since the slopes of the first and third segments are consistent within the uncertainties, we fixed these slopes to be the same in our following analysis. We then obtained the following best-fit results to the entire X-ray light curve:

- The initial decay index is  $\alpha_1 = 1.20_{-0.06}^{+0.05}$ ,
- the first break occurs at  $t_{b1} = 3.70_{-1.00}^{+0.54}$  ks, after which the decay index is  $\alpha_2 = 0.04_{-0.21}^{+0.27}$ ,
- the second break occurs at  $t_{b2} = 14.9_{-2.8}^{+5.9}$  ks and is followed by a decay index of  $\alpha_3 \equiv \alpha_1$ ,
- the third break occurs at  $t_{b3} = 354_{-103}^{+432}$  ks and is followed by a decay index of  $\alpha_4 = 1.92_{-0.25}^{+0.52}$ . (The uncertainties in the final break time and final slope were obtained by fixing  $\alpha_3 = 1.20$  and calculating the confidence region in the  $t_{b3}/\alpha_4$  plane satisfying  $\chi_{min}^2 + 4.6$ , representing a 90% confidence region for 2 interesting parameters.)

The *Chandra* data were critically important in determining the parameters of the late portion of the light curve. The fit to the third segment is dominated by the small uncertainties in the first two *Chandra* observations, which were each binned into a single point for this fit,

although we show them binned at finer time resolution in Figure 2. The last segment of the light curve depends almost entirely on the *Chandra* data for definition of the break time and slope. The overall fit has  $\chi^2 = 21.4$  for 26 degrees of freedom. By comparison, the best fit model with a single slope after 15 ks (no jet break) has  $\alpha_3 = 1.39_{-0.03}^{+0.04}$  with  $\chi^2 = 59.9$  for 26 degrees of freedom. Finally a fit with a single slope of 1.20 after 15 ks (as shown in Figure 2) has  $\chi^2 = 135$  for 27 degrees of freedom. We conclude that the third break in the light curve is required by the data.

We note that the X-ray light curve shows evidence for a strong energy injection episode in the time range (2200–30,000s), as discussed in more detail by Soderberg et al. (2006). This is the first clear evidence for energy injection into the external shock for a short GRB, and requires a mechanism for refreshing the external shock similar to those proposed for long GRBs, but operating in the context of short GRB models.

#### 4. Discussion

We interpret the last break in the X-ray light curve as a jet break. These data, based on a well-sampled and well-behaved X-ray light curve, constitute the best measurement yet of a jet break for a short GRB. The jet parameters can be obtained by fitting a model of jet evolution to the available radio, optical, and X-ray lightcurves. Following Panaitescu & Kumar (2003) and Panaitescu (2005), we model the afterglow of GRB 051221A with a uniform relativistic jet undergoing lateral expansion and interacting with a homogeneous circumburst medium. The calculation of the synchrotron emission from the electrons accelerated by the forward shock is done assuming that the distribution of the electrons with energy is a power-law and that the electron and magnetic field energies are constant fractions ( $\epsilon_e$  and  $\epsilon_B$ , respectively) of the post-shock energy. Radiative losses, the spread in the photon arrival time due to the curvature of the emitting surface, and the relativistic beaming of the radiation are taken into account. The emission from the reverse shock sweeping into the out-flowing ejecta, synchrotron self-absorption (at radio frequencies), the effect of inverse-Compton scattering on electron cooling and its contribution to the X-ray light curve are also included but, for the best-fit parameters obtained for 051221A, are not important.

The best-fit parameters are determined by minimization of  $\chi^2$  between the model fluxes and the X-ray, optical, and radio measurements. The basic jet model has six parameters: three for the jet dynamics (initial energy  $E_0$ , initial opening  $\theta_0$ , and circumburst medium density  $n$ ) and three for the jet emission (the two microphysical parameters  $\epsilon_e$  and  $\epsilon_B$ , and the slope  $-p$  of the electron distribution). The available radio, optical, and X-ray measurements determine three or four characteristics of the afterglow synchrotron emission (peak flux,

location of the injection and cooling break frequencies, and possibly the self-absorption frequency), depending on whether the self-absorption frequency is below or above the radio, which constrain  $E_0$ ,  $n$ ,  $\epsilon_e$  and  $\epsilon_B$ . The spectral slope of the optical and X-ray continua, as well as the optical and X-ray decay indices, over-constrain the electron index  $p$ . The epoch of the last break in the X-ray light curve determines primarily the initial jet opening angle. Finally, the injected kinetic energy is constrained by the flattening of the X-ray light-curve in its second segment.

Figure 3 shows two fits to the radio, optical, and X-ray measurements of the afterglow of GRB 051221A obtained with a relativistic jet interacting with a homogeneous circumburst medium and undergoing energy injection at 0.1 days (to accommodate the flattening of the X-ray light-curves at that epoch). The two fits correspond to a lower limit ( $n = 10^{-4} \text{ cm}^{-3}$ ) and an upper limit ( $n = 0.1 \text{ cm}^{-3}$ ) on the density of the ambient medium. These densities span the allowed range, as shown in the inset by the variation of the reduced  $\chi_\nu^2$  with ambient density (the remaining model parameters were left free to minimize  $\chi^2$ ). For  $n = 10^{-4} \text{ cm}^{-3}$ , which is characteristic for a binary merger occurring in the halo of the host galaxy, the jet initial opening is  $\theta_0 = 4^\circ$  and the total jet kinetic energy (after injection) is  $E_{jet} = 10^{49} \text{ erg}$ . For  $n = 0.1 \text{ cm}^{-3}$ , more typical of the interstellar medium, the jet parameters are  $\theta_0 = 8^\circ$  and  $E_{jet} = 5 \times 10^{49} \text{ erg}$ . For either case, at the epoch of energy injection ( $\sim 0.1 \text{ d}$ ), the incoming ejecta increase the forward-shock energy by a factor of 2. Also for either case, the jet deceleration and decrease of the relativistic beaming of its emission renders the boundary of the spreading jet visible to the observer at a few days, when the X-ray light-curve decay exhibits a steepening. Given the small angular offset from the center of the host galaxy and the evidence for a slight excess in  $N_H$  above the Galactic value, we favor the higher density regime.

The fits obtained using the complete X-ray light curves are not statistically acceptable ( $\chi_\nu^2 \geq 2.5$  for 43 degrees of freedom). This is largely due to the poor fit at the earliest times, when the decay rate of the pre-injection X-ray emission,  $F_x \propto t^{-1.20}$ , is faster than the model prediction. The post-break decay of the X-ray emission,  $F_x(t > 4d) \propto t^{-1.93}$ , indicates that the power-law distribution with energy of the shock-accelerated electrons has an exponent  $p = \alpha_x \simeq 2$ . Together with the average spectral energy index of the X-ray continuum,  $\beta_x \equiv \Gamma - 1 = 0.96 \pm 0.09$ , this implies that the cooling frequency is below the X-ray band (in which case  $\beta_x = p/2$ ). Then, the pre-injection decay of the X-ray light-curve should be  $F_x \propto t^{-(3p-2)/4} = t^{-0.94 \pm 0.14}$ , which is slower than observed, suggesting a departure from the standard assumptions of the jet model (e.g. a slightly evolving index  $p$  or non-uniform ambient medium density). (We refer the reader to Zhang & Mészáros (2004) for a compilation of the relations between  $\alpha_x$ ,  $\beta_x$ , and  $p$  for a variety of models, together with references to the original sources of these relationships.)



Statistically acceptable fits ( $\chi^2_\nu \approx 1.0$ ) are obtained if only the post-injection data are fit with the jet model, as shown in the inset of Figure 3. The resulting jet parameters are very similar to those obtained for the energy injection model except that the range of allowed densities extends to larger values,  $n \leq 3 \text{ cm}^{-3}$ .

The single radio flux measurement may be dominated by the reverse shock component, which depends on the Lorentz factor of the ejecta responsible for the energy injection episode. With only a single radio detection, the Lorentz factor of the incoming ejecta is not well-constrained by the data (although the injected energy can be constrained by the X-ray data). Hence the strength of the reverse shock cannot be robustly determined for this burst. Although we have arbitrarily adjusted the ejecta Lorentz factor to fit this single data point, it does not allow us to further constrain any of the afterglow parameters, including the density.

In Figure 4 we compare the initial jet angle,  $\theta_0$ , and total jet energy,  $E_{jet}$ , for GRB 051221A with those of two other short bursts, GRB 050709 and GRB 050724, and with several long bursts. For the long bursts, we show the best-fit parameters found by Panaitescu (2005) using the same numerical modelling approach used here. For GRB 050709 we show the range of values obtained for the higher density solution ( $10^{-4} \text{ cm}^{-3} < n < 0.1 \text{ cm}^{-3}$ ) found by Panaitescu (2006); a jet angle larger than most of the long GRBs in this sample is required for this case. For GRB 050724, we show the limits obtained in Paper I using our late-time *Chandra* observation that provides evidence against any jet break at less than 22 days post-burst. The jet angle we obtain for GRB 051221A is consistent with jet angles found for long GRBs (Panaitescu 2005; Frail et al. 2001; Bloom, Frail, & Kulkarni 2003), but is significantly lower than that of GRB 050724, implying a wide range in jet collimation for short bursts.

We find that GRB 051221A has a jet energy lower than that of long GRBs by an order of magnitude. The lower energy of the GRB 051221A jet is consistent with an origin from a binary merger, as in this case the mass of the debris torus formed during the merger is expected to be  $\sim 10$  times lower than that of the torus formed in the collapse of the core of massive stars. Furthermore, the lower limit of circumburst densities allowed for the short GRBs 050709 and 051221A is compatible with these bursts occurring outside their host galaxies, as expected from the large kick velocities that neutron stars can acquire at birth.

The flat portion of the light curve of GRB 051221A is very similar to flat segments seen in many long GRBs. In fact, this light curve looks very similar to that of GRB 050315 (Vaughan et al. 2006), with the notable exception that GRB 051221A has no evidence for a steeply decaying initial segment. These flat segments have been interpreted as being due to energy injection into the external shock (Nousek et al. 2006; Zhang et al. 2006; Panaitescu et al. 2006), but this is the first time that this behavior has been seen in a short GRB. As

discussed more extensively by Soderberg et al. (2006), the implication is that the external shock continues to be refreshed hours after the GRB itself, either due to continued activity from the central engine or to lower velocity shocks from the initial burst catching up with the decelerating blast wave. By contrast, GRB 050724 has a large, late bump in the X-ray light curve, interpreted as continued central engine activity (Paper I), with the post-flare afterglow returning to the same power-law decay as the pre-flare afterglow. No flares are seen in the afterglow of GRB 051221A.

## 5. Conclusions

We find that the X-ray afterglow of GRB 051221A has a break in the light curve between 2.9 and 9.1 days post-burst, from a decay index of 1.2 to  $\sim 2$ , that is consistent with being a jet break. Unfortunately, only upper limits are available in the optical and radio data following this break, so the achromaticity of the break cannot be established; however, the break can be modelled as a jet interacting with an external medium with a density in the range  $10^{-4} < n < 0.1 \text{ cm}^{-3}$ . At the low density limit we find an initial jet opening angle of  $4^\circ$  and a total jet kinetic energy of  $10^{49}$  ergs. At the higher density limit, which may be more consistent with the small offset of the afterglow from the host galaxy and with the indication of a modest amount of intrinsic X-ray absorption in the host, we find a jet angle of  $8^\circ$  and jet energy of  $5 \times 10^{49}$  ergs. We obtain a much wider range of possible circumburst densities than found by Soderberg et al. (2006) and somewhat larger jet energies (by a factor of 1.5-7), but are in agreement with their results for the remaining jet parameters. These results indicate that at least some short GRBs have afterglows collimated to angles similar to jets in long GRBs, though the jet energy can be substantially lower. Together with the lack of a jet break in GRB 050724 (Paper I), this implies a wide range of jet angles for short GRBs. Finally, the X-ray light curve of GRB 051221A has a strong energy injection signature, indicating that the energy of the external shock is increased by a factor of two at about 0.1 days after the burst.

This research was supported by NASA contract NAS5-00136, SAO grant GO6-7050A, and ASI grant I/R/039/04. We acknowledge the use of data obtained through the High Energy Astrophysics Science Archive Research Center (HEASARC) Online Service, provided by the NASA/Goddard Space Flight Center. Special thanks to Paul Plucinsky, Andrea Prestwich, and other members of the *Chandra* X-ray Center staff who helped plan and execute the *Chandra* Target of Opportunity observations across the holidays, and who performed the rapid data processing needed to schedule the entire set of observations.

## REFERENCES

- Barbier, L., et al. 2006, ApJ, in preparation
- Barthelmy, S. D., et al. 2005a, Space Science Reviews, 120, 143
- Barthelmy, S. D., et al. 2005b, Nature, 438, 994
- Bloom, J. S., Frail, D. A., & Kulkarni, S. R. 2003, ApJ, 594, 674
- Bloom, J. S., et al. 2006, ApJ, 638, 354
- Burrows, D. N., et al. 2005, Space Science Rev., 120, 165
- Burrows, D. N., Capalbi, M., & Grupe, D. 2005, GCN Circ. 4366, <http://gcn.gsfc.nasa.gov/gcn3/4366.gcn3>
- Campana, S., et al. 2006, A&A, in press
- Cummings, J., et al. 2005, GCN Circ. 4365, <http://gcn.gsfc.nasa.gov/gcn3/4365.gcn3>
- Dickey, J. M. & Lockman, F. J. 1990, ARA&A, 28, 215
- Eichler, D., Livio, M., Piran, T., & Schramm, D. N. 1989, Nature, 340, 126
- Fox, D. B., et al. 2005, Nature, 437, 845
- Frail, D.A., et al. 2001, ApJ, 562, L55
- Gehrels, N., et al. 2004, ApJ, 611, 1005
- Gehrels, N., et al. 2005, Nature, 437, 851
- Golenetskii, S., Aptekar, R., Mazets, E., Pal'shin, V., Frederiks, D., and Cline, T. 2005, GCN Circ. 4394, <http://gcn.gsfc.nasa.gov/gcn3/4394.gcn3>
- Grupe, D., Burrows, D. N., Patel, S. K., Kouveliotou, C., Zhang, B., Mészáros, P., Wijers, R. A. M., & Gehrels, N. 2006, ApJ, submitted (Paper I; astro-ph/0603773)
- Grupe, D., et al. 2005, GCN Circ. 4389, <http://gcn.gsfc.nasa.gov/gcn3/4389.gcn3>
- Hill, J.E., et al. 2004, SPIE, 5165, 217
- Hjorth, J., et al. 2005, Nature, 437, 859
- Hjorth, J., et al. 2005, ApJ, 630, L117

- Lattimer, J., & Schramm, D. 1976, *ApJ*, 210, 549
- Nousek, J., et al. 2006, *ApJ*, 642, 389
- Paczyński, B. 1986, *ApJ*, 308, L43
- Paczyński, B. 1991, *Acta Astron.*, 41, 257
- Pagani, C., et al. 2006, *ApJ*, in press (astro-ph/0603658)
- Panaitescu, A. 2005, *MNRAS*, 363, 1409
- Panaitescu, A. 2006, *MNRAS*, 367, L42
- Panaitescu, A., & Kumar, P. 2003, *ApJ*, 592, 390
- Panaitescu, A., Mészáros, P., Gehrels, N., Burrows, D., & Nousek, J. 2006, *MNRAS*, 366, 1357
- Parsons, A., et al. 2005, *GCN Circ.* 4363, <http://gcn.gsfc.nasa.gov/gcn3/4363.gcn3>
- Romano, P., et al. 2006, *A&A*, in press (astro-ph/0602497)
- Rosswog, S. 2005, *ApJ*, 634, 1202
- Rosswog, S., Ramirez-Ruiz, E., & Davies, M. B. 2003, *MNRAS*, 345, 1077
- Soderberg, A. M., et al. 2006, *ApJ*, submitted (astro-ph/0601455)
- Vaughan, S., et al. 2006, *ApJ*, 638, 920
- Villasenor, J. S., et al. 2005, *Nature*, 437, 855
- Zhang, B., & Mészáros, P. 2004, *Int. J. of Modern Phys. A*, 19, 2385
- Zhang, B., Fan, Y.Z., Dyks, J., Kobayashi, S., Mészáros, P., Burrows, D.N., Nousek, J.A., & Gehrels, N. 2006, *ApJ*, 642, 354

Table 1. *Chandra*/ACIS-S Observation Log for GRB 051221A

ObsID	Date	T <sub>start</sub> (UT)	T <sub>end</sub> (UT)	T <sub>elapse</sub> <sup>1</sup>	T <sub>exp</sub> (ks)
6681	22 Dec 2005	13:55:20	22:51:11	0.13	29.8
7256	25 Dec 2005	12:17:00	21:13:04	0.38	29.8
7257	5 Jan 2006	05:49:54	11:30:12	1.31	17.9
7258	10 Jan 2006	02:11:17	09:44:07	1.73	24.6
6683	16 Jan 2006	01:17:58	15:19:44	2.24	48.5

<sup>1</sup>T<sub>elapse</sub> = T<sub>start</sub> – T<sub>0</sub> (in Ms), where T<sub>0</sub> is the burst trigger time (01:51:16 UT on 21 December 2005).

Table 2. Power law spectral fits to the X-ray data of GRB 051221A

	Γ	N <sub>H</sub> <sup>1</sup>	χ <sup>2</sup> /ν	Flux <sup>2</sup>
<i>Swift</i> /XRT (WT mode)	2.2 ± 0.4	1.7 <sup>+1.0</sup> <sub>-0.9</sub>	22.5 / 15	<sup>3</sup>
<i>Swift</i> /XRT (PC mode) <sup>4</sup>	2.1 ± 0.2	1.8 <sup>+0.7</sup> <sub>-0.5</sub>	13.5 / 30	<sup>3</sup>
<i>Chandra</i> /ACIS-S	1.94 <sup>+0.29</sup> <sub>-0.19</sub>	1.4 ± 0.9	17.2 / 22	
<i>Chandra</i> /ACIS-S #6681	1.88 <sup>+0.16</sup> <sub>-0.23</sub>	1.3 <sup>+0.9</sup> <sub>-0.8</sub>	15.4 / 18	1.7
<i>Chandra</i> /ACIS-S #7256	2.07 <sup>+0.36</sup> <sub>-0.33</sub>	1.4 ( <i>frozen</i> )	1.6 / 4	0.46

<sup>1</sup>Absorption column density in units of 10<sup>21</sup> cm<sup>-2</sup>. The Galactic column density along this line of sight is 6.7 × 10<sup>20</sup> cm<sup>-2</sup> (Dickey & Lockman 1990).

<sup>2</sup>Flux units are 10<sup>-13</sup> erg cm<sup>-2</sup> s<sup>-1</sup> for the 0.3–10 keV energy band.

<sup>3</sup>Flux is not quoted for XRT data because it changes rapidly during these observation intervals (see Fig. 2 for flux vs. time).

<sup>4</sup>PC mode data from T+501 s to T+65721 s, excluding the first portion, which is piled up.

Table 3. X-ray light curves for GRB 051221A

$T_{start}$ (ks)	$T_{end}$ (ks)	Flux (erg cm <sup>-2</sup> s <sup>-1</sup> )	Instrument / Mode
0.092	0.112	$(1.46 \pm 0.22) \times 10^{-10}$	<i>Swift</i> XRT / WT
0.112	0.132	$(1.95 \pm 0.21) \times 10^{-10}$	<i>Swift</i> XRT / WT
0.132	0.152	$(1.58 \pm 0.19) \times 10^{-10}$	<i>Swift</i> XRT / WT
0.152	0.172	$(1.25 \pm 0.17) \times 10^{-10}$	<i>Swift</i> XRT / WT
0.172	0.192	$(8.98 \pm 1.74) \times 10^{-11}$	<i>Swift</i> XRT / WT
0.192	0.212	$(1.08 \pm 0.19) \times 10^{-10}$	<i>Swift</i> XRT / WT
0.212	0.252	$(8.62 \pm 1.17) \times 10^{-11}$	<i>Swift</i> XRT / WT
0.252	0.332	$(5.47 \pm 0.84) \times 10^{-11}$	<i>Swift</i> XRT / WT
0.301	0.401	$(4.74 \pm 0.66) \times 10^{-11}$	<i>Swift</i> XRT / PC
0.401	0.501	$(2.97 \pm 0.53) \times 10^{-11}$	<i>Swift</i> XRT / PC
0.501	0.701	$(2.44 \pm 0.33) \times 10^{-11}$	<i>Swift</i> XRT / PC
0.701	0.901	$(2.17 \pm 0.31) \times 10^{-11}$	<i>Swift</i> XRT / PC
0.901	1.101	$(1.06 \pm 0.22) \times 10^{-11}$	<i>Swift</i> XRT / PC
1.101	1.301	$(9.32 \pm 2.03) \times 10^{-12}$	<i>Swift</i> XRT / PC
1.301	1.701	$(8.87 \pm 1.40) \times 10^{-12}$	<i>Swift</i> XRT / PC
1.701	2.101	$(6.43 \pm 1.20) \times 10^{-12}$	<i>Swift</i> XRT / PC
2.101	2.501	$(4.88 \pm 1.04) \times 10^{-12}$	<i>Swift</i> XRT / PC
6.101	7.101	$(2.95 \pm 0.51) \times 10^{-12}$	<i>Swift</i> XRT / PC
7.101	8.101	$(2.31 \pm 0.45) \times 10^{-12}$	<i>Swift</i> XRT / PC
12.10	13.10	$(3.13 \pm 0.53) \times 10^{-12}$	<i>Swift</i> XRT / PC
13.10	14.10	$(2.49 \pm 0.47) \times 10^{-12}$	<i>Swift</i> XRT / PC
17.40	18.78	$(2.09 \pm 0.35) \times 10^{-12}$	<i>Swift</i> XRT / PC
18.78	19.91	$(1.72 \pm 0.33) \times 10^{-12}$	<i>Swift</i> XRT / PC
23.27	31.48	$(1.53 \pm 0.17) \times 10^{-12}$	<i>Swift</i> XRT / PC
34.97	43.05	$(1.19 \pm 0.15) \times 10^{-12}$	<i>Swift</i> XRT / PC
46.99	54.62	$(7.63 \pm 1.29) \times 10^{-13}$	<i>Swift</i> XRT / PC
57.77	65.71	$(6.34 \pm 1.01) \times 10^{-13}$	<i>Swift</i> XRT / PC
75.13	77.76	$(5.56 \pm 1.18) \times 10^{-13}$	<i>Swift</i> XRT / PC
81.55	93.55	$(5.05 \pm 1.04) \times 10^{-13}$	<i>Swift</i> XRT / PC
93.55	105.55	$(3.98 \pm 0.92) \times 10^{-13}$	<i>Swift</i> XRT / PC
110.5	135.5	$(2.21 \pm 0.43) \times 10^{-13}$	<i>Swift</i> XRT / PC

Table 3—Continued

$T_{start}$ (ks)	$T_{end}$ (ks)	Flux (erg cm <sup>-2</sup> s <sup>-1</sup> )	Instrument / Mode
139.9	164.3	$(2.11 \pm 0.44) \times 10^{-13}$	<i>Swift</i> XRT / PC
167.9	199.2	$(1.24 \pm 0.29) \times 10^{-13}$	<i>Swift</i> XRT / PC
202.7	233.9	$(1.49 \pm 0.33) \times 10^{-13}$	<i>Swift</i> XRT / PC
237.4	268.6	$(1.23 \pm 0.29) \times 10^{-13}$	<i>Swift</i> XRT / PC
272.1	303.3	$(9.48 \pm 2.52) \times 10^{-14}$	<i>Swift</i> XRT / PC
307.3	337.8	$(8.02 \pm 2.35) \times 10^{-14}$	<i>Swift</i> XRT / PC
341.5	424.8	$(6.17 \pm 1.35) \times 10^{-14}$	<i>Swift</i> XRT / PC
428.3	511.5	$(3.63 \pm 1.07) \times 10^{-14}$	<i>Swift</i> XRT / PC
515.1	597.6	$(3.66 \pm 1.12) \times 10^{-14}$	<i>Swift</i> XRT / PC
601.9	943.7	$(1.66 \pm 0.40) \times 10^{-14}$	<i>Swift</i> XRT / PC
944.1	1199.9	$< 1.68 \times 10^{-14}$	<i>Swift</i> XRT / PC
130.9	136.3	$(1.85 \pm 0.19) \times 10^{-13}$	<i>Chandra</i> ACIS
136.3	141.8	$(1.79 \pm 0.18) \times 10^{-13}$	<i>Chandra</i> ACIS
141.8	148.2	$(1.56 \pm 0.16) \times 10^{-13}$	<i>Chandra</i> ACIS
148.2	154.8	$(1.51 \pm 0.15) \times 10^{-13}$	<i>Chandra</i> ACIS
154.8	161.1	$(1.44 \pm 0.15) \times 10^{-13}$	<i>Chandra</i> ACIS
384.1	393.6	$(5.15 \pm 0.75) \times 10^{-14}$	<i>Chandra</i> ACIS
393.6	404.0	$(4.69 \pm 0.68) \times 10^{-14}$	<i>Chandra</i> ACIS
404.0	414.3	$(4.49 \pm 0.67) \times 10^{-14}$	<i>Chandra</i> ACIS
1311.9	1329.8	$(4.64 \pm 1.65) \times 10^{-15}$	<i>Chandra</i> ACIS
1726.7	1751.3	$(3.20 \pm 1.18) \times 10^{-15}$	<i>Chandra</i> ACIS
2247.8	2296.3	$(1.57 \pm 0.61) \times 10^{-15}$	<i>Chandra</i> ACIS

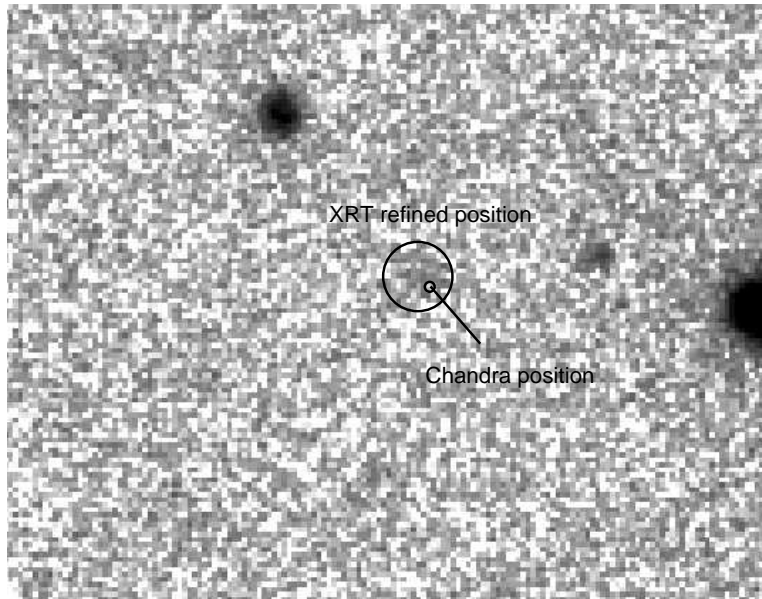


Fig. 1.— XRT and *Chandra* error circles plotted over the UVOT/UVW1-band image (narrow band UV filter centered at 251 nm; 3.3 ks integration) of the GRB field.



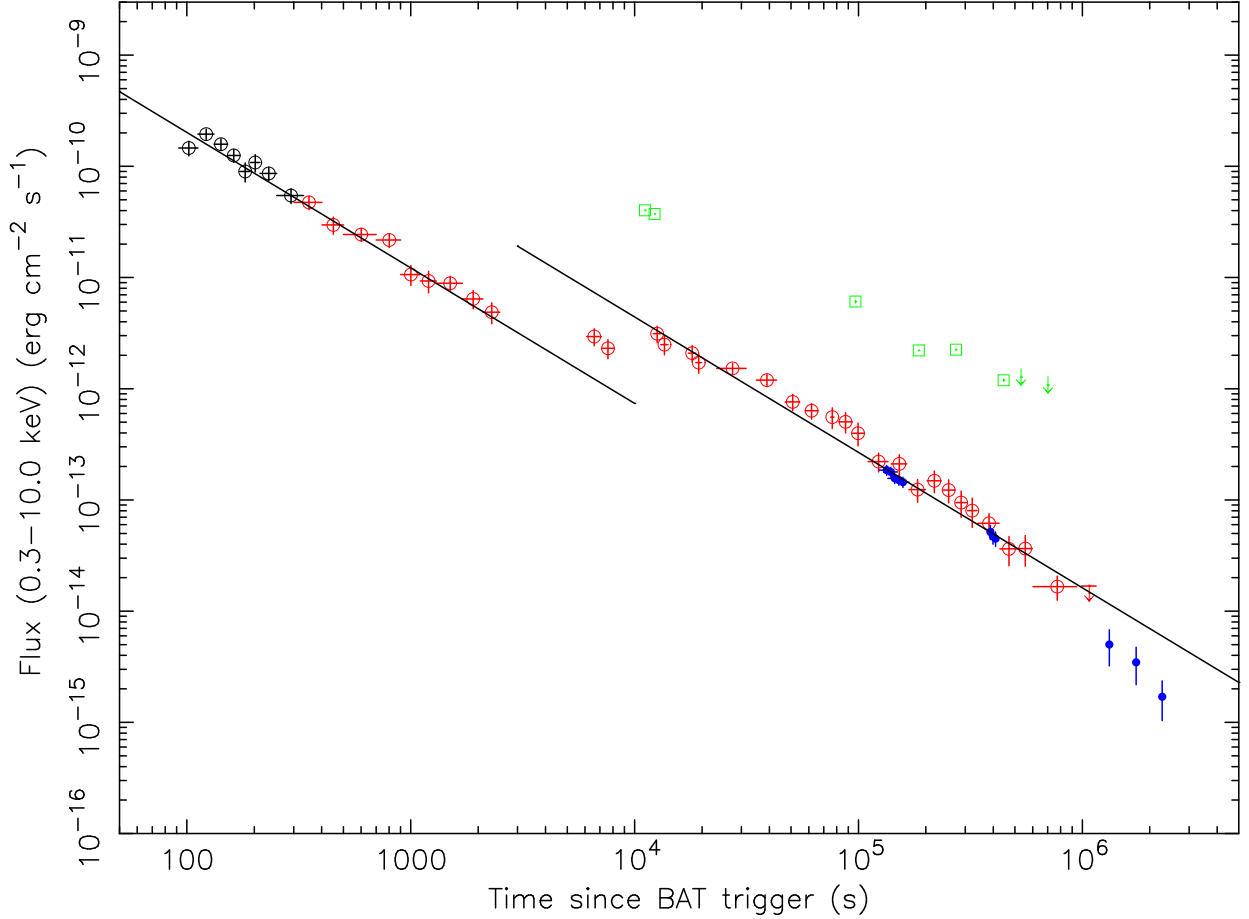


Fig. 2.— Combined *Swift* XRT and *Chandra* ACIS-S light curve of the afterglow of GRB051221A. The light curve shows the 0.3–10.0 keV unabsorbed flux. Black circles indicate the WT mode XRT data at early times. Red circles indicate the PC mode XRT data. Blue dots indicate the *Chandra* observations at late times. Green squares (arrows) indicate the  $r'$  band measurements (upper limits) from Soderberg et al. (2006), arbitrarily scaled for comparison with the X-ray data. The black lines have slopes of  $-1.20$ , determined from a three segment fit to the data up to  $T_0 + 360$  ks with the first and third decay indices tied together (see §3.3). The X-ray light curve deviates from the late power law after the last  $r'$ -band detection.

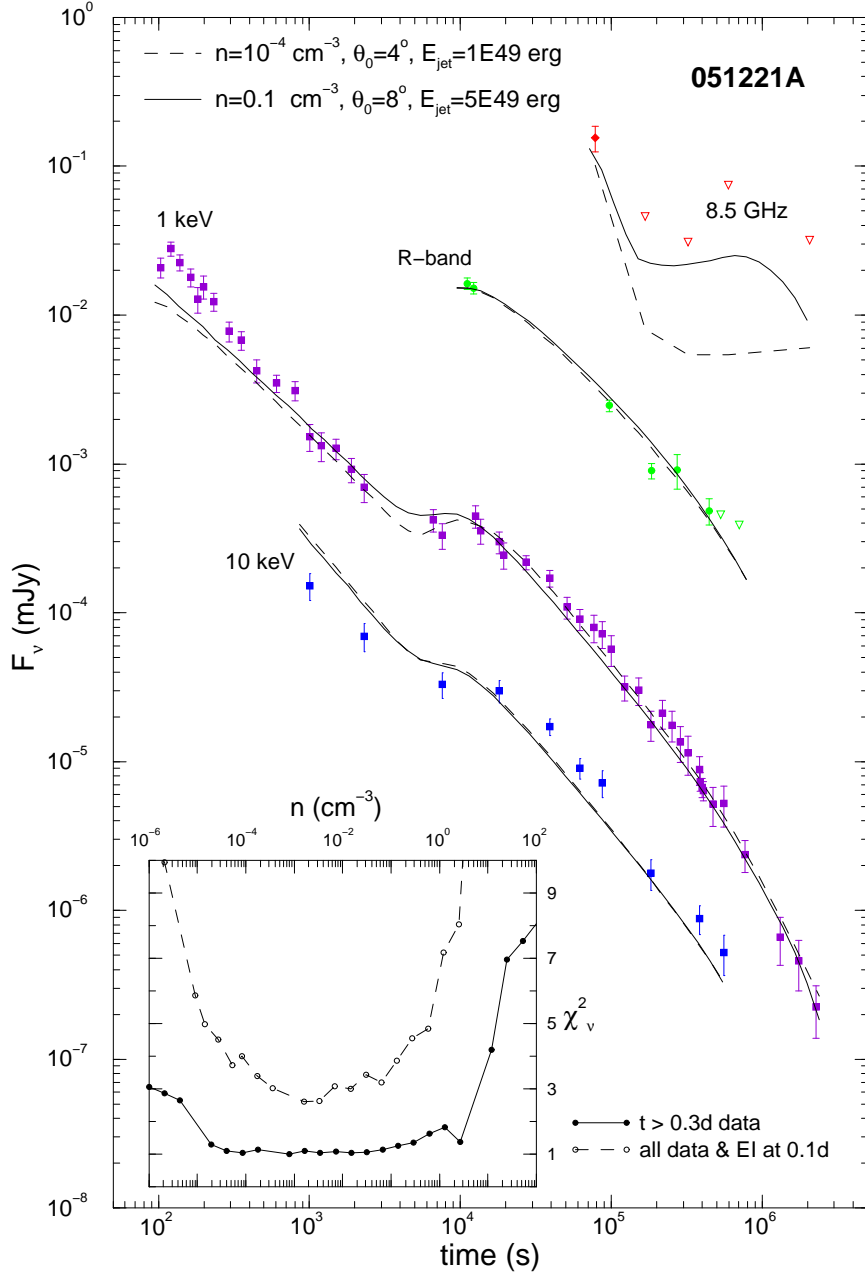


Fig. 3.— Examples of fits to the multiwavelength measurements of GRB afterglow 051221A obtained with the jet model and an episode of energy injection in the blast wave. The low density fit ( $n = 10^{-4} \text{ cm}^{-3}$ ) is shown with dashed curves, the higher density fit ( $n = 0.1 \text{ cm}^{-3}$ ) with continuous lines. The radio and optical data points are taken from Soderberg et al. (2006). Triangles indicate  $2\sigma$  radio upper limits. (The fits also included  $i'$  band and  $z'$  band data, which are omitted from this figure for clarity). Inset: variation of  $\chi^2_\nu$  with circumburst medium density (in protons  $\text{cm}^{-3}$ ) for the model fits. The dashed line is for a fit to all of the data, including an energy injection episode commencing at about 4000 s. Better fits are obtained with the jet model without energy injection if only the data after the X-ray flattening are fitted (solid line). Similar jet parameters are obtained in both cases.

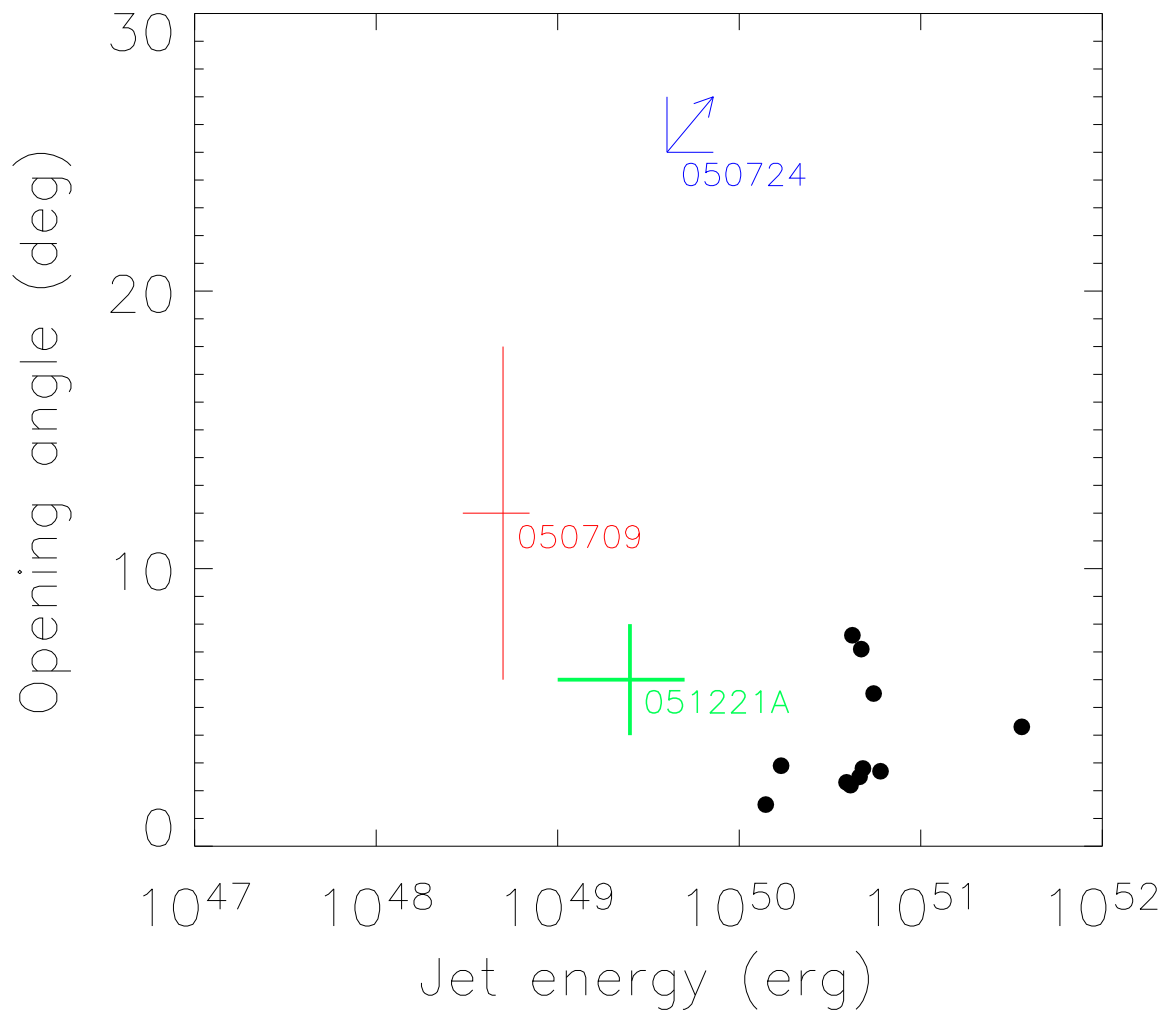


Fig. 4.— Opening jet angle  $\theta_0$  and jet energy  $E_{jet}$  for several long and short GRBs. The black dots indicate values obtained for the long GRBs 980519, 990123, 990510, 991216, 000301c, 000926, 010222, 011211, 020813, 030226 (all from Panaitescu 2005, using the same method employed here), and 030329 (previously unpublished result obtained with the same method). Results for three short GRBs are also plotted. For GRB 050709 (red), we show the range of values allowed for the high density case obtained by Panaitescu (2006). For GRB 050724 (blue) we show the lower limits obtained by Grupe et al. (2006). Both  $\theta_0$  and  $E_{jet}$  have lower limits, which are indicated by the horizontal and vertical lines with the angled arrow. The range of values found here for GRB 051221A is shown in green.